Phase-Difference-Dependent Surface Plasmon Polariton Waveguide Coupling in a Symmetrical Dual-Channel Metal-Insulator-Metal Structure

Qilin Ma [ID], Haoming Bao, Gang Zhang, Jiaosheng Li [ID], Maosheng Yang, and Min Kong

Abstract—**This work reports a phase difference modulated coupling of two surface plasmon polariton (SPP) sources in a symmetrical two-channel metal-insulator-metal (MIM) waveguide device. In the device, two sources with different initial phases interact indirectly through the function of a rectangular cavity. With the phase difference varying, we have achieved tunable SPP coupling followed by continuously adjustable filtering property and Fano resonance. Further results show that the tunable SPP coupling in the resonance cavity can be well described by the electromagnetic wave interference theory. Moreover, we have also demonstrated the excellent performance of this phase-difference-dependent MIM waveguide in refractive-index sensing and have achieved considerable sensitivity as high as 818.8 nm/RIU. This research has great significance for tunable filtering and signal compensation in MIM waveguide-based photonic chips and also provides a device with high potential in refractive-index sensing.**

Index Terms—**Surface plasmon polaritons, MIM waveguide, fano resonance, phase difference.**

I. INTRODUCTION

AS TRADITIONAL chips reach their computing bottleneck, alternative new photonic chips have received much attention due to their high computing efficiency [1], [2], [3], [4], [5], [6], [7]. Photonic chips have a theoretical operating speed of a million times that of current electronic chips. Mainstream research on all-optical integrated chips mainly focuses on photonic crystals and metal-insulator-metal (MIM) plasmonic waveguides [8], [9], [10], [11], [12], [13]. Among them, the MIM plasmonic waveguide overcomes the optical diffraction limit,

does not require a complex periodic structure, and is integrated easily into small devices [14], [15], [16], [17], [18]. Therefore, it has become one of the most important representatives of the current all-optical integrated chips and attracted much attention [14], [15], [18], [19], [20].

For MIM waveguides, surface plasmon polaritons (SPPs) are usually applied as the source. They are evanescent waves that can manipulate light at a sub-wavelength scale. With the development of micro/nano fabrication technologies, SPP properties in MIM waveguide devices with various micro/nano structures have been widely studied [16], [21], [22], [23], [24], [25], [26], [27], [11], including the filtering effect [16], plasmon-induced transparency (PIT) effects [26], [27], Fano resonance effects [11], etc. These phenomena open up the applications of the MIM waveguide, such as slow light devices, refractive index sensors, photonic chips, and so on. For the all-optical integrated chip, MIM waveguide devices based on these phenomena can also realize logic gate functions [28], [29], [30]. However, the previous results show that these devices usually have low efficiencies due to the short propagation distance caused by the high energy consumption [28], [29], and this greatly limits the actual application of them. An energy compensation strategy by adding a secondary source could overcome this problem. It highly requires a good understanding of SPP interactions in the MIM waveguide. However, as far as we know, the studied SPP interactions usually apply identical SPP sources with the same phase. Interactions between SPP sources with different phases could bring new phenomena and provide new opportunities for applications. Unfortunately, such phase-difference-dependent SPP interaction in the MIM waveguide has not been reported yet.

In this paper, we report the interaction (or coupling) between two phase-different SPP sources in a MIM waveguide with two bus slots and a rectangular cavity. Thereinto, the bus slots are used for SPP channels, and the cavity is used as the medium for the interaction of the sources. With adjusting the phase difference of the sources, tunable SPP coupling has been achieved, thereby enabling the continuously modulated filtering characteristics and Fano resonance. This phase-different-dependent SPP coupling can be well described by the electromagnetic wave interference theory. Last but not the least, we have also demonstrated the good refractive-index sensing performance of this MIM waveguide with high sensitivity of 818.8 nm/RIU.
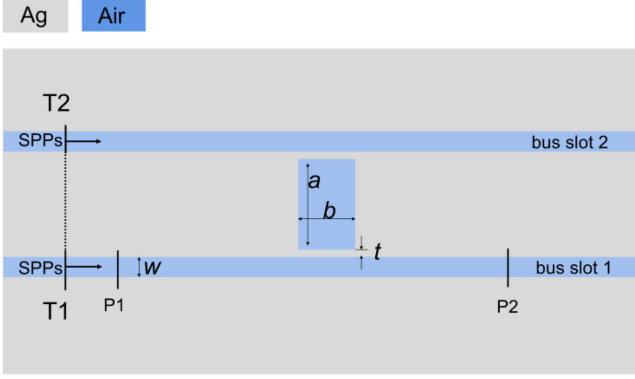
Fig. 1.   Structure diagram of the MIM waveguide with dual-channels.

Fig. 2.   (a) Transmission spectra achieved at P2 with only one source in slot 1. (b-c) |Hz| field distribution excited at (b) 578 nm and (c) 815 nm.

II. STRUCTURE AND THEORETICAL MODEL

Fig. 1 shows the up-down symmetrical structure of the designed MIM waveguide with two bus slots and a rectangular cavity. The waveguide coupling mode theory is usually utilized for analyzing the coupling of the resonant cavity and the waveguide slots in the MIM waveguide [14], [16], [31]. Air is chosen as the insulator with a dielectric constant $\varepsilon_d = 1$, in the further simulation. The dielectric function of the metal Ag is described by the Drude model:

$$\varepsilon_m\,(\omega) = \varepsilon_\infty - \frac{\omega_p^2}{\omega\,(\omega + i\gamma)} \quad (1)$$

where ω is angular frequency of the incident light, ε_∞ is the dielectric constant of Ag at the infinite angular frequency, ω_{p} is bulk plasma frequency, γ is the damping frequency of the oscillations, and i is the unit imaginary, respectively. Corresponding values of these parameters for the further simulation are as following: $\varepsilon_\infty = 3.7$, $\omega_p = 1.38 \times 10^{16}$ Hz, and $\gamma = 2.73 \times 10^{13}$ Hz [31], [32]. Since the width of waveguide slot is far less than the incident light wavelength, only fundamental TM mode can be excited [33]. The dispersion relation of the fundamental TM mode in a MIM waveguide is given by [33], [34]:

$$\varepsilon_d k_m + \varepsilon_m k_d \tan h\left(\frac{k_d}{2}w\right) = 0 \quad (2)$$

with the wavenumbers of the dielectric (k_m) and the metal (k_d) defined as:

$$k_d = \sqrt{\beta^2 - \varepsilon_d k_0^2}$$

$$k_m = \sqrt{\beta^2 - \varepsilon_m k_0^2} \quad (3)$$

where $k_0 = \lambda_0/2\pi$ is the free space wave vector, $n_{eff} = \beta/k_0$ is the effective dielectric constant, and β is the propagation constant of SPPs in the MIM structure.

III. SIMULATION RESULTS AND DISCUSSIONS

Finite-difference time-domain (FDTD) method was applied for the simulation with steps kept at $\Delta x = \Delta y = 5$ nm [35]. Beca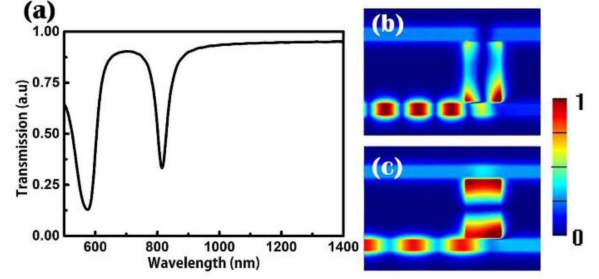use SPP waveguides can break through the diffraction limit and have a long propagation distance in the visible to near-infrared band, they have been studied for signal regulation in the visible to near-infrared band. To facilitate the analysis of different modes, it should be ensured that a is not equal to b the main parameter is set as follows: the cavity size is $a \times b = 300$ nm $\times$ 200 nm, the widths of the two bus waveguide slots are both $w = 50$ nm, and the distances between the two waveguide slots and the resonant cavity are both $t = 20$ nm [16]. Such a slots-cavity distance can ensure a strong coupling between the bus waveguide and the cavity [31]. The two SPP sources have the same distance from them to the cavity (see the dotted line in Fig. 1). Two power monitors are set at P1 and P2 to detect the power of incident and the transmission wave, respectively. In the simulation, the amplitudes of the two sources are normalized, namely the amplitude of the two beams are the same. The transmission (T) is defined to be the ratio of powers at P1 and P2 [36].

To investigate the resonance modes of the waveguide cavity, only one SPPs source was excited at first. According to the structural symmetry, the slot 1 was considered. The results show that there are two resonance modes located at 578 nm and 815 nm, respectively, as shown in Fig. 2(a). The |Hz| field distributions excited at 578 nm and 815 nm are shown in Fig. 2(b) and (c), respectively. It can be seen that the two resonance modes occur along with the sides of a and b, respectively. It should be noted that the filtering efficiency is not as good as the reported one with one bus slot [31], and this should be attributed to the enhanced transmission by bus slot 2 in this case.

According to the standing wave theory, when the wavelength of SPPs waveguide is equal to the resonant wavelength of the cavity, the resonance conditions of the cavity can be given by:

$$\frac{4\pi Re\,(n_{eff})\,L_{eff}}{\lambda} + \varphi = 2N\pi,\ (N = 1, 2, 3\ldots) \quad (4)$$

where L_{eff} is the effective cavity length, and φ is the phase shift caused by the reflection of the cavity wall during a round trip, and Re (n_{eff}) is the real part of the effective dielectric constant n_{eff} which can be obtained by the (1)–(3) and $n_{eff} = \beta/k_0$. Admittedly, there exist higher order resonant modes (that means $N > 1$) in the certain cavity, but only the first order mode can be observed in our studied wavelength region (500–1400 nm). Therefore, when the L_{eff} equal to a and b, two intrinsic modes at 815 nm and 578 nm are investigated, respectively, as shown in Fig. 2(a).
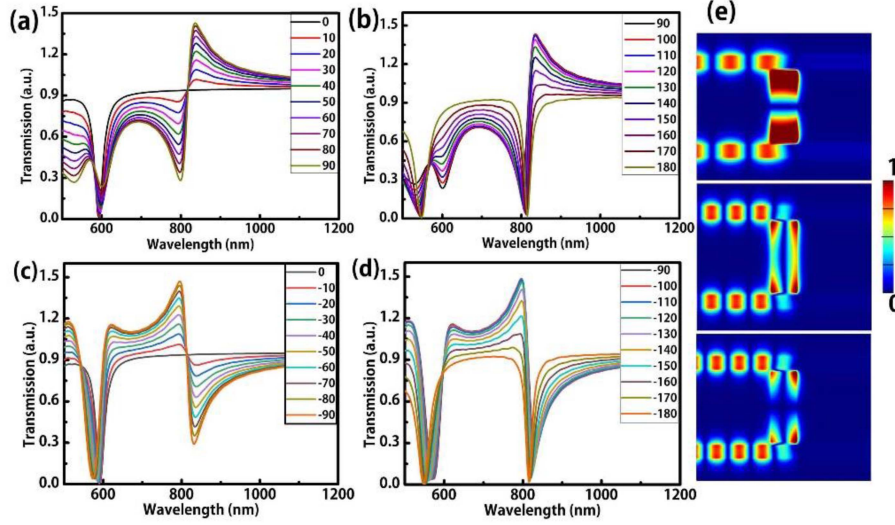
Fig. 3. Transmission spectra achieved at P2 with phase difference from (a) 0 to 90°, (b) 90° to 180°. (c) 0 to −90°, (d) −90 to −180°. (e) |Hz| field distributions excited at 815 nm (upper panel), 578 nm (middle panel) and 548 nm (lower panel). The upper panel was achieved with a phase difference of 0, and the middle panel as well as the lower panel were achieved with phase difference of 180°.

To investigate the interaction properties between two SPP sources through the cavity, the two sources were excited at the same time with a given phase difference of $\Delta\alpha = \alpha_2 - \alpha_1$ (α_1 and α_2 are the initial phases of source 1 and 2, respectively). Here we assume that the two waveguide sources are coherent, that is, $\Delta\alpha$ is constant. The data show that the transmission spectra pattern evolves with the variation of the phase differences [see Fig. 3(a)–(d)], indicating the phase-difference-dependent SPP coupling. From which it can be seen that there is only one transmission dip at $\Delta\alpha = 0$, but two dips at $\Delta\alpha = 180°$. More importantly, three transmission dips at 548, 578 and 815 nm can be observed in these patterns, and here we call them mode c mode b and mode a, respectively. For the mode a (or the dip at 815 nm), its strength decreases in the $\Delta\alpha$ range from −180° to 0 and increase in the $\Delta\alpha$ range from 0 to 180°, with a tunable transmission from 0 to 0.9. These evolved transmission spectra suggest the continuously adjustable transmission-filtering characteristics of this phase-difference dependent MIM waveguide device. For the modes b and c (or the dips at 578 nm and 548 nm), the transmission pattern show opposite evolutions to that of mode a, that is their strength increases in the $\Delta\alpha$ range from −180° to 0 but decrease at the $\Delta\alpha$ range from 0 to 180°. It should be noted that mode c and mode b seriously overlap in the range of −180° to 180° due to their very close dip positions.

To further understand the resonance modes, the |Hz| field distributions excited at different dip positions were mapped. The |Hz| field distributions show that the dips at 815 nm and 578 nm are indeed mode a and mode b, and the new dip at 548 nm (or mode c) corresponds to a quadrupole-like oscillation mode, as shown in Fig. 3(e). The mode c could be attributed to a higher order resonant mode that red-shifting into the studied wavelength region due to the SPP coupling.

To understand the dip strength evolution, let us to make some theoretical considerations. As we know, two beams of light at any point in the resonator can be expressed as:

$$E_1 = \cos(\alpha_1 + kz_1 - \omega t)$$
$$E_2 = \cos(\alpha_2 + kz_2 - \omega t) \tag{5}$$

where α_1 and α_2 represent the initial phase of the two sources, respectively, kz_1 and kz_2 represent the space phase, respectively, and t refer to time.

For these two SPP waves, which apparently have the same direction of E within our waveguide slot, are full coherent at the same frequency. According to electromagnetic wave superposition principle, the vibrational expression of the two SPPs at any point in the cavity can be expressed as:

$$E = E_1 + E_2 = \cos(\alpha_1 + kz_1 - \omega t) + \cos(\alpha_2 + kz_2 - \omega t) \tag{6}$$

thus the amplitude expression is given by:

$$A = \sqrt{1 + 1 + 2\cos(\Delta\alpha + kz_1 - kz_2)}$$

or

$$A^2 = 4\cos^2(\Delta\alpha_0/2) \tag{7}$$

where $\Delta\alpha_0 = \alpha_1 - \alpha_2 + kz_1 - kz_2$ is the phase difference of the two waves propagate to the point. Since the two bus waveguide slots are symmetric with the resonator cavity, the two SPPs have the same phases when they spread to the resonator cavity. For the mode a and mode c, the two SPPs have a space phase difference of $kz_1 - kz_2 = 180°$ due to their path difference of half round resonance trip (that is $\Delta\alpha_0 = \alpha_1 - \alpha_2 + 180°$) at the reflective wall (i.e., the b sides). Let $\Delta\alpha = \alpha_1 - \alpha_2$, while for the mode b, the two SPPs have the same phases ($kz_1 - kz_2 = 0$) at the resonant positions (that is $\Delta\alpha_0 = \Delta\alpha$). Therefore, at the resonant position, there are:

$$A_1^2 = A_3^2 = 2 + 2\cos(\Delta\alpha + 180°) \tag{8}$$
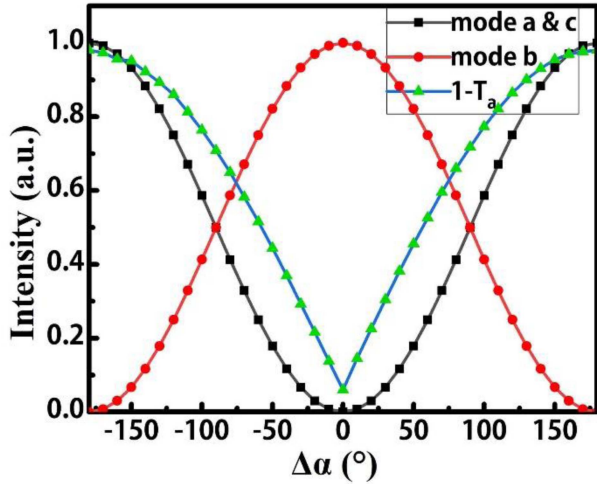$$A_2^2 = 2 + 2\cos(\Delta\alpha) \tag{9}$$

Fig. 4.   Theoretical amplitudes of the three modes versus the initial phase difference, and the simulated intensity curve of mode a denoted by $1-T_a$ (T_a is the transmittance of mode a).

Fig. 5.   The Fano parameter q is an odd function of the phase-difference $\Delta\alpha$ with a period of 360°.

where A_1, A_2 and A_3 are the amplitudes of mode a, mode b and mode c, respectively. Fig. 4 shows the theoretical amplitude evolution of these modes with $\Delta\alpha$, according to the above (8)–(9). It can well describe the spectral changes in Fig. 3(a)–(d), where mode a and mode c have the same evolution while mode b has an opposite one. In particular, when $\Delta\alpha = 0$, only mode b can be observed, and the $\Delta\alpha = 180$ °, mode a and c emerge while mode b is invisible. The simulated intensity curve of mode a denoted by $1-T_a$ (T_a is the transmittance of mode a) varies with $\Delta\alpha$, as shown in the triangle symbol curve in Fig. 4. It can be seen that $1-T_a$ and mode a have the same trend of intensity change, but the changing speeds are different especially near zero. This mainly due to the phase changes of the mode profile in Fig. 3(e) where the profile moves from positive to negative around the zero crossing causing the asymmetry between the top and lower guides. Thus, the slope of transmittance $1-T_a$ at about 0 degrees changed abruptly (like the triangle symbol curve in Fig. 4). In addition, when the $\Delta\alpha = \pm180°$, the intensity of mode a reaches the maximum, and the transmittance T_a is the smallest, while the asymmetric property is the weakest around $\pm180°$, so T_a shows a similar trend of slope variation to the mode a.

Additionally, we notice the dip at 815 nm (mode a) shows a typical Fano resonance line shape. In general, Fano resonance is generated by the symmetry break of the structures, such as H-shaped, and E-shaped, disk rings and cascade cavity nanostructures [37], [38], [39]. The Fano resonance phenomenon can be described by the Fano parameter q, as described by [40], [41]:

$$T = 1 - D\frac{(\beta + q)^2}{1 + \beta^2}$$

where D is a factor related to the continuum phase shift, and $\beta = (E - E_0)/\Gamma$ (E and E_0 represent the photon energy and resonance energy, respectively, and Γ is the line width). Fig. 5 shows the q value calculated from Fig. 3(a)–(d) is an odd function versus the $\Delta\alpha$ and slightly decreases but then dramatically
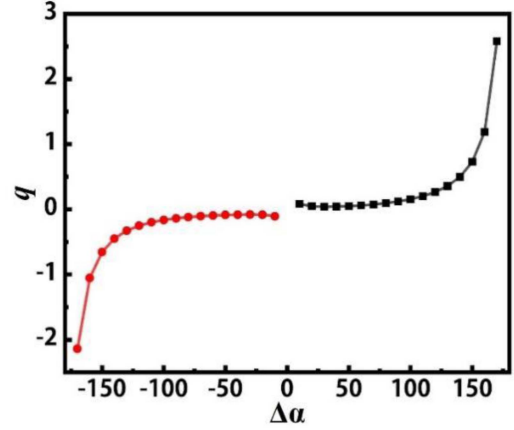
increases in the $\Delta\alpha$ range of 0 to 180°. This suggests the tunable Fano resonance is also achieved in this MIM structure. And due to the phase changes of the mode profile in Fig. 3(e) where the profile moves from positive to negative around the zero crossing causing the asymmetry between the two guides and then get q value with the opposite sign on both sides of zero.

The Fano resonance line shape should be attributed to the interference of phase-different the two sources. Different from that conventional Fano resonance occurs via the interference between a discrete resonance state and a continuum state, this case demonstrates it occurs between two states with similar line widths. Although (8)-(9) can well explain the dip intensity corresponding to the resonance wavelength, they cannot describe the Fano resonance here due to the unconsidered relationship between the phase and the wavelength. The relationship between phase and wavelength in a resonance mode is given by [42]: $\tan\alpha = -\Gamma E/(E_0^2 - E^2)$ and thus, we can achieve the E values of the two SPPs in the cavity with given phase differences, as shown in Fig. 6. Although a more precise method to solve the Fano line needs consideration of the average effect in time-domain, we consider the time the one source (SPP1) has an initial phase of 0 due to the simplified calculation. Here, the two SPPs have the same resonance position at 815 nm, same line width of 0.6 eV, and different phases (0, 180° and 100°) from it. When $\Delta\alpha = 0$, the electric fields from the two SPPs have destructive interference, resulting in the disappearing of tip and a q value of 0, as shown in Fig. 6(a). When $\Delta\alpha = 180°$, the electric fields have the same phases and thus have a constructive interference, resulting in a perfect Lorentz line shape (or an infinite q value), as shown in Fig. 6(b). When $\Delta\alpha \neq 0$, ($\Delta\alpha = 100°$ for example) both constructive and destructive interferences coexist and depend on the wavelength, asymmetric Fano line shape of the transmission is generated, as typically shown in Fig. 6(c). It is conceivable that the q value evolves with the change of the $\Delta\alpha$. It should be noted that if the precise method considering the average effect, the achieved transmission spectra could be closer to that in Fig. 3(a)–(d). In addition, for modes b and c, the asymmetric peak shapes are also shown in Fig. 3(a)–(d), which means that the Fano phenomenon of the two modes can
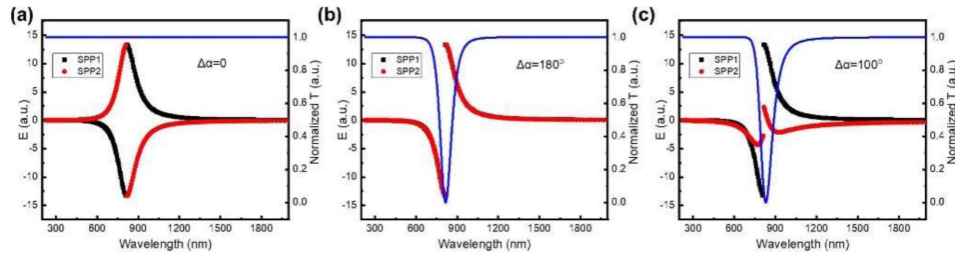
Fig. 6.   Theoretical E amplitude and transmission versus the wavelength with $\Delta\alpha$ of (a) 0, (b) 180°, and (c) 100°.
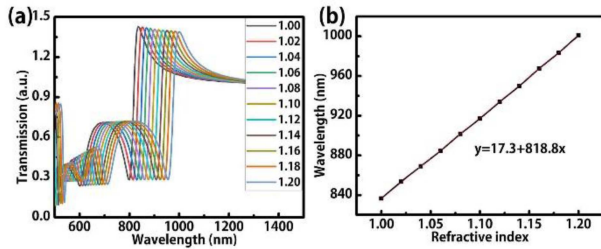

Fig. 7.   Refractive index sensing performance of this MIM plasmonic waveguide. (a) Transmission spectra achieved with environmental refractive index varies from 1.00 to 1.20 at fixed phase difference of 90°. (b) the peak position of Fano line with the refractive index varies from 1.00 to 1.20.

appear. This should be acceptable because these two modes also follow the similar electromagnetic superposition principle of mode a. However, the peaks of the two modes (b and c) are very close in wavelength and interfere with each other. This makes the difficult to discuss them individually. Therefore, we mainly discuss the Fano resonance properties of mode a here.

In addition, the Fano resonance induced peaks show hugely enhanced transmittance range from 94% to 143% at 836 nm with phase difference from 0 (or 180) to 90 degree, and from 94% to 148% at 797 nm with phase difference from 0 (or −180) to −90 degree, as shown in Fig. 4(a)–(d). And can be tuned by the phase difference. Which means that the MIM plasmonic waveguide energy can be injected through the phase difference modulation between the external waveguide source and the main waveguide source, which can solve the problem of the transmission distance of the MIM waveguide chip. This suggests the phase-difference-dependent MIM waveguide device has great signal compensation for the application in photonic chips.

Last but not the least, we studied the refractive index sensing performance of this MIM plasmonic waveguide. In general, Fano resonance is used in refractive index sensors and other applications due to its sensitivity to the environmental refractive index [40], [43]. Here we choose the case with the strongest peak (i.e., $\Delta\alpha = 90°$) to study the sensor performance of the device. The data show that the achieved transmission spectra have a holistic redshift and stable line shapes with the increase of the refractive index (n), as shown in Fig. 7(a). Moreover, quantitatively, the position of dip of mode b has a very good linear relationship with the refractive index [see Fig. 7(b)], indicating the good quantitation for the sensing. The corresponding sensitivity ($\Delta\lambda/\Delta n$) is as high as 818.8 nm/RIU, and this is a considerable value among the reported cases. These

suggests the high potential of this phase difference-dependent MIM plasmonic waveguide in refractive-index sensing.

IV. CONCLUSION

This paper has investigated the interaction properties of two SPPs sources with different phase differences in the MIM waveguide structure with a rectangle cavity. By changing the phase difference between the two SPP sources, we achieved continuous adjustable filtering and the Fano resonance properties in this MIM waveguide device. Further results show that this SPP coupling follows the electromagnetic wave superposition principle. Moreover, we have also demonstrated the excellent performance of this MIM waveguide in refractive-index sensing, with an achieved sensitivity of 818.8 nm/RIU. This work reveals the different phase-modulated SPP coupling in MIM waveguides which opens up a new opportunity for applications in replenishing the energy of the SPPs in MIM waveguide photonic chips, achieving continuously optical filtering, and refractive-index sensors.

REFERENCES

[1] M. Pelusi et al., "Photonic-chip-based radio-frequency spectrum analyser with terahertz bandwidth," *Nature Photon.*, vol. 3, no. 3, pp. 139–143, 2009.

[2] M. H. Khan et al., "Ultrabroad-bandwidth arbitrary radiofrequency waveform generation with a silicon photonic chip-based spectral shaper," *Nature Photon.*, vol. 4, no. 2, pp. 117–122, 2010.

[3] W.-C. Lai, S. Chakravarty, X. Wang, C. Lin, and R. T. Chen, "On-chip methane sensing by near-IR absorption signatures in a photonic crystal slot waveguide," *Opt. Lett.*, vol. 36, no. 6, pp. 984–986, 2011.

[4] A. Arriola et al., "Low bend loss waveguides enable compact, efficient 3D photonic chips," *Opt. Exp.*, vol. 21, no. 3, pp. 2978–2986, 2013.

[5] E. Kuramochi et al., "Large-scale integration of wavelength-addressable all-optical memories on a photonic crystal chip," *Nature Photon.*, vol. 8, no. 6, pp. 474–481, 2014.

[6] V. Brasch et al., "Photonic chip–based optical frequency comb using soliton Cherenkov radiation," *Science*, vol. 351, no. 6271, pp. 357–360, 2016.

[7] P. J. Cegielski et al., "Monolithically integrated perovskite semiconductor lasers on silicon photonic chips by scalable top-down fabrication," *Nano Lett.*, vol. 18, no. 11, pp. 6915–6923, 2018.

[8] B. Corcoran et al., "Green light emission in silicon through slow-light enhanced third-harmonic generation in photonic-crystal waveguides," *Nature Photon.*, vol. 3, no. 4, pp. 206–210, 2009.

[9] Y. Gong, L. Wang, X. Hu, X. Li, and X. Liu, "Broad-bandgap and low-sidelobe surface plasmon polariton reflector with Bragg-grating-based MIM waveguide," *Opt. Exp.*, vol. 17, no. 16, pp. 13727–13736, 2009.

[10] C. Xiong et al., "Slow-light enhanced correlated photon pair generation in a silicon photonic crystal waveguide," *Opt. Lett.*, vol. 36, no. 17, pp. 3413–3415, 2011.

[11] J. Qi et al., "Independently tunable double Fano resonances in asymmetric MIM waveguide structure," *Opt. Exp.*, vol. 22, no. 12, pp. 14688–14695, 2014.

[12] D. Li, K. Du, S. Liang, W. Zhang, and T. Mei, "Wide band dispersionless slow light in hetero-MIM plasmonic waveguide," *Opt. Exp.*, vol. 24, no. 20, pp. 22432–22437, 2016.

[13] D. Headland, X. Yu, M. Fujita, and T. Nagatsuma, "Near-field out-of-plane coupling between terahertz photonic crystal waveguides," *Optica*, vol. 6, no. 8, pp. 1002–1011, 2019.

[14] J. Tao, X. G. Huang, and J. H. Zhu, "A wavelength demultiplexing structure based on metal-dielectric-metal plasmonic nano-capillary resonators," *Opt. Exp.*, vol. 18, no. 11, pp. 11111–11116, May 2010.

[15] H. Lu, X. M. Liu, L. R. Wang, Y. K. Gong, and D. Mao, "Ultrafast all-optical switching in nanoplasmonic waveguide with Kerr nonlinear resonator," *Opt. Exp.*, vol. 19, no. 4, pp. 2910–2915, Feb. 2011.

[16] H. Lu, X. M. Liu, Y. K. Gong, D. Mao, and L. R. Wang, "Enhancement of transmission efficiency of nanoplasmonic wavelength demultiplexer based on channel drop filters and reflection nanocavities," *Opt. Exp.*, vol. 19, no. 14, pp. 12885–12890, Jul. 2011.

[17] H. Wang et al., "Tunable band-stop plasmonic waveguide filter with symmetrical multiple-teeth-shaped structure," *Opt. Lett.*, vol. 41, no. 6, pp. 1233–1236, Mar. 2016.

[18] W. L. Barnes, A. Dereux, and T. W. Ebbesen, "Surface plasmon subwavelength optics," *Nature*, vol. 424, no. 6950, pp. 824–830, Aug. 2003.

[19] S. I. Bozhevolnyi, V. S. Volkov, E. Devaux, J. Y. Laluet, and T. W. Ebbesen, "Channel plasmon subwavelength waveguide components including interferometers and ring resonators," *Nature*, vol. 440, no. 7083, pp. 508–511, Mar. 2006.

[20] M. Zhang and Z. Wang, "Analytical method for metal-insulator-metal surface plasmon polaritons waveguide networks," *Opt. Exp.*, vol. 27, no. 1, pp. 303–321, 2019.

[21] B. Rothenhäusler and W. Knoll, "Surface–plasmon microscopy," *Nature*, vol. 332, no. 6165, pp. 615–617, 1988.

[22] J. Homola, S. S. Yee, and G. Gauglitz, "Surface plasmon resonance sensors," *Sensors Actuators B: Chem.*, vol. 54, no. 1/2, pp. 3–15, 1999.

[23] M. I. Petrov, S. V. Sukhov, A. A. Bogdanov, A. S. Shalin, and A. Dogariu, "Surface plasmon polariton assisted optical pulling force," *Laser Photon. Rev.*, vol. 10, no. 1, pp. 116–122, 2016.

[24] A. Agrawal, S. H. Cho, O. Zandi, S. Ghosh, R. W. Johns, and D. J. Milliron, "Localized surface plasmon resonance in semiconductor nanocrystals," *Chem. Rev.*, vol. 118, no. 6, pp. 3121–3207, 2018.

[25] Z. Yin et al., "Hybrid Au–Ag nanostructures for enhanced plasmon-driven catalytic selective hydrogenation through visible light irradiation and surface-enhanced Raman scattering," *J. Amer. Chem. Soc.*, vol. 140, no. 3, pp. 864–867, 2018.

[26] G. Cao et al., "Formation and evolution mechanisms of plasmon-induced transparency in MDM waveguide with two stub resonators," *Opt. Exp.*, vol. 21, no. 8, pp. 9198–9205, Apr. 2013.

[27] T. Wang, Y. Zhang, Z. Hong, and Z. Han, "Analogue of electromagnetically induced transparency in integrated plasmonics with radiative and subradiant resonators," *Opt. Exp.*, vol. 22, no. 18, pp. 21529–21534, Sep. 2014.

[28] H. Wei, Z. Wang, X. Tian, M. Käll, and H. Xu, "Cascaded logic gates in nanophotonic plasmon networks," *Nature Commun.*, vol. 2, 2011, Art. no. 387.

[29] Y. Fu, X. Hu, C. Lu, S. Yue, H. Yang, and Q. Gong, "All-optical logic gates based on nanoscale plasmonic slot waveguides," *Nano Lett.*, vol. 12, no. 11, pp. 5784–5790, Nov. 2012.

[30] A. Dolatabady and N. Granpayeh, "All-optical logic gates in plasmonic metal–insulator–metal nanowaveguide with slot cavity resonator," *Proc. SPIE*, vol. 11, 2017, Art. no. 026001.

[31] Q. Zhang, X.-G. Huang, X.-S. Lin, J. Tao, and X.-P. Jin, "A subwavelength coupler-type MIM optical filter," *Opt. Exp.*, vol. 17, no. 9, pp. 7549–7554, 2009.

[32] J. Tao, X. G. Huang, X. Lin, Q. Zhang, and X. Jin, "A narrow-band subwavelength plasmonic waveguide filter with asymmetrical multiple-teeth-shaped structure," *Opt. Exp.*, vol. 17, no. 16, pp. 13989–13994, 2009.

[33] J. A. Dionne, L. A. Sweatlock, H. A. Atwater, and A. Polman, "Plasmon slot waveguides: Towards chip-scale propagation with subwavelength-scale localization," *Phys. Rev. B*, vol. 73, no. 3, 2006, Art. no. 035407.

[34] B. Wang and G. P. Wang, "Plasmon Bragg reflectors and nanocavities on flat metallic surfaces," *Appl. Phys. Lett.*, vol. 87, no. 1, 2005, Art. no. 013107.

[35] W. Bing and P. W. Guo, "Surface plasmon polariton propagation in nanoscale metal gap waveguides," *Opt. Lett.*, vol. 29, no. 17, pp. 1992–1994, 2004.

[36] X.-S. Lin and X.-G. Huang, "Tooth-shaped plasmonic waveguide filters with nanometeric sizes," *Opt. Lett.*, vol. 33, no. 23, pp. 2874–2876, 2008.

[37] B. Yuan, W. Zhou, and J. Wang, "Novel H-shaped plasmon nanoresonators for efficient dual-band SERS and optical sensing applications," *J. Opt.*, vol. 16, no. 10, 2014, Art. no. 105013.

[38] B. Sun et al., "Tunable Fano resonance in E-shape plasmonic nanocavities," *J. Phys. Chem. C*, vol. 118, no. 43, pp. 25124–25131, 2014.

[39] G. Lin et al., "Ultra-compact high-sensitivity plasmonic sensor based on Fano resonance with symmetry breaking ring cavity," *Opt. Exp.*, vol. 27, no. 23, pp. 33359–33368, 2019.

[40] M. F. Limonov, M. V. Rybin, A. N. Poddubny, and Y. S. Kivshar, "Fano resonances in photonics," *Nature Photon.*, vol. 11, no. 9, pp. 543–554, 2017.

[41] L. Gu et al., "Fano resonance lineshapes in a waveguide-microring structure enabled by an air-hole," *APL Photon.*, vol. 5, no. 1, 2020, Art. no. 016108.

[42] J. Zuloaga and P. Nordlander, "On the energy shift between near-field and far-field peak intensities in localized plasmon systems," *Nano Lett.*, vol. 11, no. 3, pp. 1280–1283, 2011.

[43] M. Rahmani, B. Luk'Yanchuk, and M. Hong, "Fano resonance in novel plasmonic nanostructures," *Laser Photon. Rev.*, vol. 7, no. 3, pp. 329–349, 2013.